



# Unlocking efficient and robust ozone decomposition with CNT-confined manganese oxide via synergistic electronic modulation

Bin Liu, Ziran Yi, Yunjun Yang, Yatai Li, Jingling Yang\*, Mingshan Zhu\*

Guangdong Key Laboratory of Environmental Pollution and Health, School of Environment, Jinan University, Guangzhou 511443, PR China



## ARTICLE INFO

### Keywords:

Ozone decomposition  
MnO<sub>2</sub> confined in CNT  
Space confinement  
Interfacial electronic interaction  
Rate-determining step

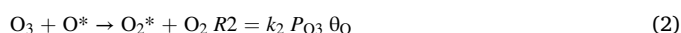
## ABSTRACT

Manganese oxides (MnO<sub>2</sub>)-based catalysts are prominent candidates for ozone elimination, which always bear the accumulation of the intermediate oxygen species and water, resulting in unsatisfactory catalytic efficiency. To overcome this critical defect, we propose carbon nanotubes confined MnO<sub>2</sub> catalysts (MnO<sub>2</sub>-in-CNT) for efficient and stable ozone decomposition over a wide relative humidity range (RH, 15–90%). Strikingly, the catalyst exhibits an efficient and sustainable ozone conversion (98%) over 100 h under a gas hourly space velocity (GHSV) of 600,000 mL g<sup>-1</sup> h<sup>-1</sup> and RH of 15%, and durability under high RH (77% over 50 h, RH 70%), well beyond its unconfined analog and most reported works. This excellent catalytic performance can be attributed to the facilitated intermediate desorption on active sites and the confined structure alleviated the effect of water on inner MnO<sub>2</sub>. This discovery is expected to drive great progress in the applications of confined-structure catalysts for air purification.

## 1. Introduction

Ground-level ozone, as a highly toxic gas, has become one of the major airborne pollutants [1,2]. Ozone is primarily derived from the photochemical reactions between nitrogen oxides (NO<sub>x</sub>) and volatile organic compounds (VOCs), or the emissions from the modern house-hold equipment, such as photocopiers and ultraviolet disinfection [3,4]. It is known that long-term exposure to ozone, even at low concentration levels (>100 ppb), is detrimental to both the ecosystems and human health [5–7]. Therefore, it is urgent to develop the safe, efficient and economical ozone elimination methods.

Currently, heterogeneous catalytic decomposition is the most promising method due to its higher efficiency, lower cost, as well as feasibility at room temperature attracting considerable attention [8]. Among various catalysts, manganese oxides (MnO<sub>2</sub>) have been deemed as the most active catalysts for the ozone elimination among diversified transition metal oxide catalysts [9–12]. In addition, a conventional catalytic ozone decomposition process over manganese-based catalysts proceeds by the following equations:



where  $R$  corresponds to the reaction rate,  $*$  means the active site,  $P_{\text{O}_3}$  represents the ozone partial pressure,  $\theta$  refers to the fraction of total active sites, and  $k$  denotes the constant. In general, the rate ( $R$ ) of step (1) is much faster than that of step (2) and step (3), with the slowest step (3) becomes the rate-determining step [13,14]. Under the identical  $P_{\text{O}_3}$ , the rate of all the steps depends on the fraction of total active sites ( $\theta$ ) available to react with the reactants (Eqs. 1–3). The slow desorption of the peroxide species to gaseous oxygen during the step (3) results in the accumulation of peroxide species at the active sites of the catalyst, thus decreasing the overall efficiency of the ozone decomposition [14,15]. The accumulation of the surface peroxide and the water-induced deactivation remain two crucial obstacles for the practical application of the manganese-based catalysts in the ozone decomposition.

In fact, great efforts have been made to overcome these two challenges [16–18]. For example, Zhang et al. utilized the synergy effect of Mn and Co in (Mn, Co)<sub>3</sub>O<sub>4</sub> to accelerate the rate-determining steps [14]. Besides, Zhu et al. encapsulated the  $\alpha$ -MnO<sub>2</sub> nanofiber with the hydrophobic graphene shells to hinder the chemisorption of water vapour, thereby enhancing its water resistance [19]. Although the reported methods improved the decomposition performance and the water tolerance to a certain extent, the catalytic performance still remains to be boosted further. Therefore, there is a great environmental and

\* Corresponding authors.

E-mail addresses: [yangjl@jnu.edu.cn](mailto:yangjl@jnu.edu.cn) (J. Yang), [zhumingshan@jnu.edu.cn](mailto:zhumingshan@jnu.edu.cn) (M. Zhu).

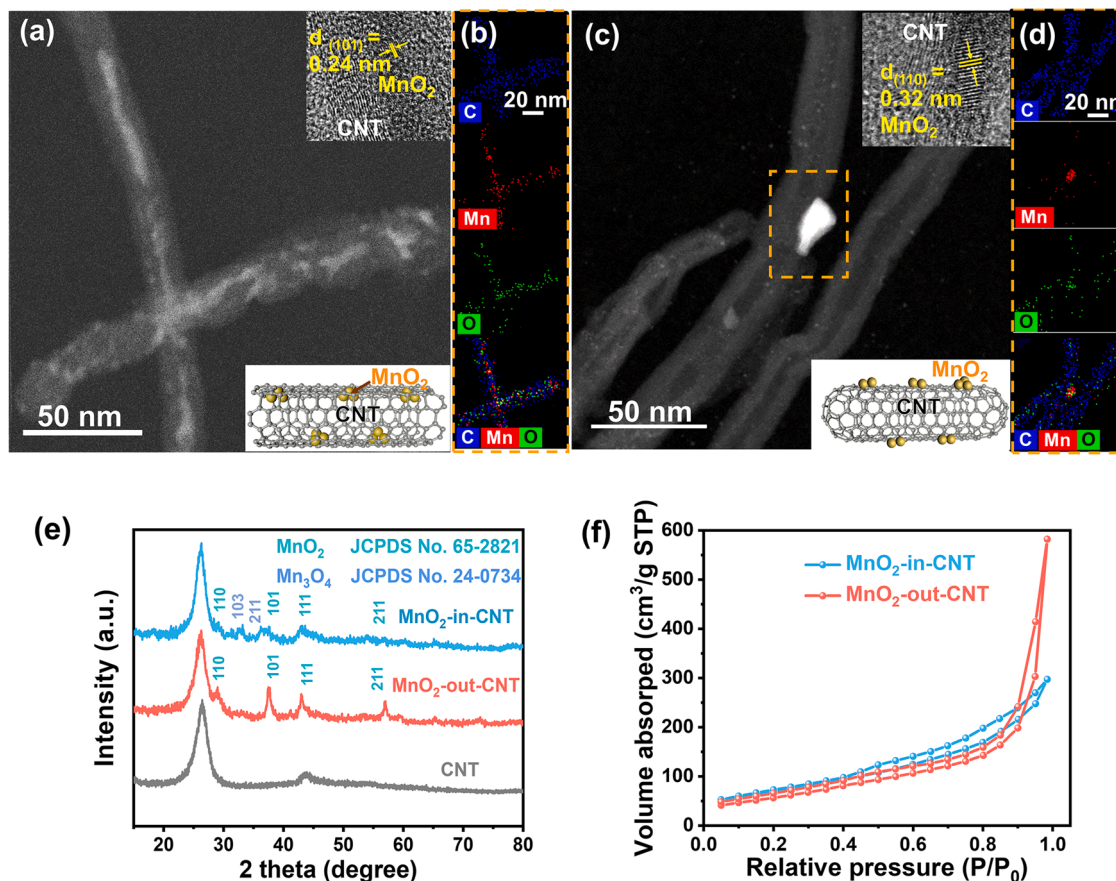


**Fig. 1.** HADDF-STEM image, (Insets) HRTEM images and element mapping images of (a, b) MnO<sub>2</sub>-in-CNT and (c, d) MnO<sub>2</sub>-out-CNT. (e) XRD patterns of CNT, MnO<sub>2</sub>-in-CNT and MnO<sub>2</sub>-out-CNT. (f) N<sub>2</sub> adsorption-desorption isotherms of MnO<sub>2</sub>-in-CNT and MnO<sub>2</sub>-out-CNT.

economic demand to develop cost-effective catalytic materials with high activity, strong stability and excellent humidity resistance.

The confinement of the catalytic center inside the nanoscale space, as is reported, could lead to unique intermolecular arrangements that lower the activation energy barrier and alter the stability of certain reactions, which have significant effects on the catalytic performance [20–22]. A variety of different types of confined-structure catalysts (such as the nanopores or nanoholes in porous architectures [23], the nanochannels in tubular structures [24], as well as the van der Waals gaps in layered materials [25]) have been exploited. Among them, carbon nanotubes (CNTs) have well-defined hollow interiors and exhibit outstanding mechanical as well as electron conductivity [26,27]. Recently, special attention has been directed to CNT-confined catalysts owing to the catalytic reaction benefits significantly from proceeding within a nano-sized CNTs reaction vessel, where the activity and stability exceed that on the outside of the nanotubes by more than an order of magnitude [27–29]. Inspired by this, it might be reasonable to expect that the encapsulation of the manganese-based catalysts into the CNT cavities can show greater redox activity and stability. However, the performance of the confined-structure catalysts on the catalytic ozone decomposition still remains elusive.

On this view, we herein take a confined-structure catalyst that encapsulated the MnO<sub>2</sub> nanoparticles into CNT (MnO<sub>2</sub>-in-CNT) to improve the activity and stability of the ozone decomposition in a wide humidity range. As expected, the catalyst exhibited ultra-high catalytic stability over a wide humidity range (15 ~ 90%). Under a gas hourly space velocity (GHSV) of 600,000 mL g<sup>-1</sup> h<sup>-1</sup> and relative humidity (RH) of 15%, the ozone conversion efficiency was as high as 98% over 100 h, showing excellent stability. Even though the RH increased to 70%, the ozone conversion also reached up to 77% over 50 h, far

exceeding its unconfined analog (MnO<sub>2</sub>-out-CNT and bare MnO<sub>2</sub>) and the most reported works. Furthermore, this cost-effective system can simultaneously decompose O<sub>3</sub> and VOCs, thus realizing the air purification. Combining FTIR, XPS results and density functional theory (DFT) calculations, it is observed that the ozone decomposition over MnO<sub>2</sub>-in-CNT occurs not only the surface of the MnO<sub>2</sub> in the confined space, but also on the nearby exterior surface of CNT, due to the changed surface electronic properties through the interfacial electron modulation. The barrier of the rate-determining steps (peroxides desorption) in MnO<sub>2</sub>-in-CNT is significantly lower than those of the single MnO<sub>2</sub>. Additionally, the confined structure protected the active sites on the inner MnO<sub>2</sub> against the water-induced deactivation and the catalyst deterioration during the ozone decomposition.

## 2. Experimental section

### 2.1. Synthesis of MnO<sub>2</sub>-in-CNT and MnO<sub>2</sub>-out-CNT

Synthesis of MnO<sub>2</sub>-in-CNT membrane: Raw CNT was firstly refluxed in HNO<sub>3</sub> (68 wt%) at 130 °C for 12 h [30]. The resulting CNT was functionalized with carbonyl groups with open ends. After being filtered and washed with ultrapure water until neutral pH, the products were lyophilized. Afterwards, 134 µL of Mn(NO<sub>3</sub>)<sub>2</sub> (50 wt%) was dissolved in 3.2 mL ethanol and then added dropwise to 200 mg of the pre-treated CNT. The mixed solution was treated by ultrasonication for 1 h, then stirred for 4 h, and dried at room temperature. The obtained products were gradually heated to 300 °C in air and kept for 2 h. The obtained sample is denoted as MnO<sub>2</sub>-in-CNT. Subsequently, the sample was dispersed in ethanol (0.1 g sample / 3 mL ethanol) and dropwisely coated onto a commercial poly tetra fluoroethylene (PTFE) filter

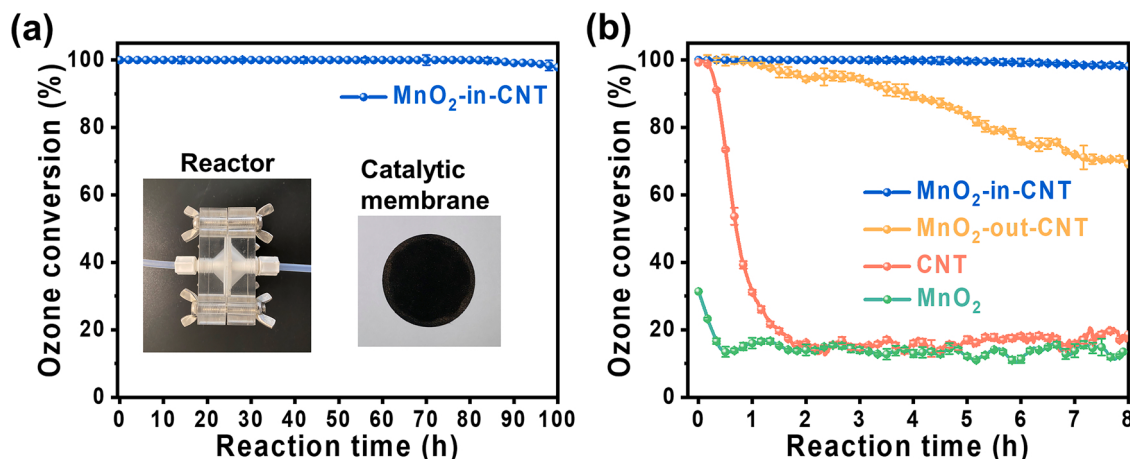


**Fig. 2.** (a) Ozone conversion of the supported catalyst. Inset: Photo of MnO<sub>2</sub>-in-CNT loaded on the PTFE membrane, (b) Ozone conversion performance of samples under 15% RH.

membrane ( $D = 47$  mm, pore size = 5  $\mu\text{m}$ ) to obtain the catalytic membrane.

Synthesis of MnO<sub>2</sub>-out-CNT membrane: For MnO<sub>2</sub>-out-CNT sample, CNT with closed caps was used, which were obtained by refluxing raw CNT in HNO<sub>3</sub> (37 wt%) solution at 110 °C for 5 h. Afterwards, MnO<sub>2</sub> deposited on the close capped CNT was prepared and loaded onto porous PTFE membrane under the identical procedures as MnO<sub>2</sub>-in-CNT. The obtained sample was labeled as MnO<sub>2</sub>-out-CNT membrane.

## 2.2. Catalytic activity tests

The catalytic activity for the ozone decomposition was evaluated at room temperature (25 °C) in a continuous flow membrane reactor with the as-prepared catalytic membrane fixed in the catalytic membrane reactor by O-rings (Fig. S1a and b). O<sub>3</sub> was generated from an ozone generator (CH-ZTW3G, China) with clean air as oxygen source. During reaction, the O<sub>3</sub> gas continuously passed through the catalytic membrane reactor. The RH was adjusted by passing compressed dry N<sub>2</sub> through a constant water bath bubbler to mix with the O<sub>3</sub> gas, the value of RH was measured by a hygrometer (Elitech, GSP-6, China). The total gas flow was kept at 1000 mL min<sup>-1</sup>, and the inlet O<sub>3</sub> concentration was kept at 50 ppm. The inlet and outlet O<sub>3</sub> concentration was detected by an O<sub>3</sub> detector (model 106-L, 2B Technologies). The conversion of ozone was calculated using the following equation:

$$\text{O}_3 \text{ removal rate} = (C_{\text{in}} - C_{\text{out}}) / C_{\text{in}} \times 100\% \quad (4)$$

where  $C_{\text{in}}$  and  $C_{\text{out}}$  are inlet and outlet concentrations of O<sub>3</sub>, respectively.

## 3. Results and discussion

### 3.1. Characterization of MnO<sub>2</sub>-in-CNT

We respectively deposited MnO<sub>2</sub> nanoparticles inside and outside of the CNTs, denoted as MnO<sub>2</sub>-in-CNT and MnO<sub>2</sub>-out-CNT as catalysts for ozone removal. The synthesis process of MnO<sub>2</sub>-in-CNT and MnO<sub>2</sub>-out-CNT is illustrated in Fig. S2. The TEM images (Fig. S4 and S5) and detailed analysis on high-angle annular dark-field mode (HAADF) STEM (Fig. S6 and Fig. 1) clearly demonstrate the successful confinement of MnO<sub>2</sub> nanoparticles in the tubes (inner diameter of ca. 8 nm) of CNT in MnO<sub>2</sub>-in-CNT, while the MnO<sub>2</sub> in MnO<sub>2</sub>-out-CNT deposited on the CNT exterior surface. The element mapping result of MnO<sub>2</sub>-in-CNT (Fig. 1b) demonstrates the material confined in CNTs is manganese oxide, while its crystallinity was confirmed by powder X-ray diffraction (XRD) (Fig. 1e), high-resolution transmission electron microscopy (HRTEM) images inset (Fig. 1a) and selected area electron diffraction (SAED)

pattern (Fig. S7). The XRD patterns (Fig. 1e and S8) show that both MnO<sub>2</sub>-out-CNT and MnO<sub>2</sub>-in-CNT exhibit characteristic diffraction peaks of the (002) and (100) crystal planes of CNT (JCPDS No. 65–6212) and diffraction peaks of (110), (101), (111), (211) corresponding to  $\beta$ -MnO<sub>2</sub> (JCPDS No. 65–2821), the weak peaks at 32.4° and 36.1° assigned to (103) and (211) planes of Mn<sub>3</sub>O<sub>4</sub> (JCPDS No. 24–0734) were also detected. The results indicate that slight amount of reduced oxide-Mn<sub>3</sub>O<sub>4</sub> coexists in the sample MnO<sub>2</sub>-in-CNT, attributing to the strong interaction between encapsulated MnO<sub>2</sub> and interior wall of CNT walls [30,31]. The (002) plane of CNT and the (101) plane of MnO<sub>2</sub> were observed in HRTEM results. The Raman spectra of MnO<sub>2</sub>-in-CNT and MnO<sub>2</sub>-out-CNT show two bands centered at 1584 cm<sup>-1</sup> and 1356 cm<sup>-1</sup> (Fig. S9), corresponding to the characteristic E<sub>2g</sub> and D modes of carbon nanotubes, respectively [32]. The Raman band centered at 637 cm<sup>-1</sup> is attributed to the Mn-O bond vibrations [33]. However, for MnO<sub>2</sub>-in-CNT, the Mn-O band is weaker, which may be due to the encapsule of the MnO<sub>2</sub> in CNT [19].

The weight percentage of MnO<sub>2</sub> and CNTs in MnO<sub>2</sub>-in-CNT and MnO<sub>2</sub>-out-CNT were analyzed by TG-DSC (Fig. S10). It is calculated that the amount of MnO<sub>2</sub> in both MnO<sub>2</sub>-in-CNT and MnO<sub>2</sub>-out-CNT samples was ca. 24 wt%, corresponding to the Mn/C molar ratio of 1:23. The accurate content of Mn in the MnO<sub>2</sub>-in-CNT and MnO<sub>2</sub>-out-CNT was determined to be 15.5% and 15.1%, respectively, revealing the MnO<sub>2</sub> ratio is ca 0.24.5 wt% and 23.9 wt%. The results were in good agreement with the experimental results of TG-DSC. The N<sub>2</sub> adsorption-desorption isotherms are shown in Fig. 1f, the MnO<sub>2</sub>-in-CNT exhibits higher surface area ( $S_{\text{BET}} = 250.374 \text{ m}^2 \text{ g}^{-1}$ ) and narrower pore volume ( $0.428 \text{ cm}^3 \text{ g}^{-1}$ ) than that of MnO<sub>2</sub>-out-CNT ( $S_{\text{BET}} = 212.549 \text{ m}^2 \text{ g}^{-1}$ ,  $0.859 \text{ cm}^3 \text{ g}^{-1}$ ) due to the open-capped CNT and the MnO<sub>2</sub> accommodate inside the channels of CNTs in MnO<sub>2</sub>-in-CNT. The element states of samples were analyzed by X-ray photoelectron spectroscopy (XPS). The Mn 2p<sub>2/3</sub> peak of MnO<sub>2</sub>-in-CNT and MnO<sub>2</sub>-out-CNT can be deconvoluted into three peaks with the binding energy at 641.6, 642.6 and 643.6 eV, corresponding to Mn<sup>2+</sup>, Mn<sup>3+</sup> and Mn<sup>4+</sup>, indicating the multiple valence states of Mn (Fig. S11). Furthermore, the structure and surface component of MnO<sub>2</sub>-in-CNT (Fig. S12) and MnO<sub>2</sub>-out-CNT (Fig. S13) catalyst after long-term reaction were examined by XRD and XPS (Mn 2p). As shown in Fig. S12, there was no significant variation before and after the reaction, indicating the excellent stability of MnO<sub>2</sub>-in-CNT.

### 3.2. Ozone catalytic activity

To ascertain the effect of the confinement on ozone decomposition. A continuous-flow membrane reactor is used to evaluate the catalytic performance of ozone decomposition ( $\text{GHSV} = 600,000 \text{ mL g}^{-1} \text{ h}^{-1}$ ) at

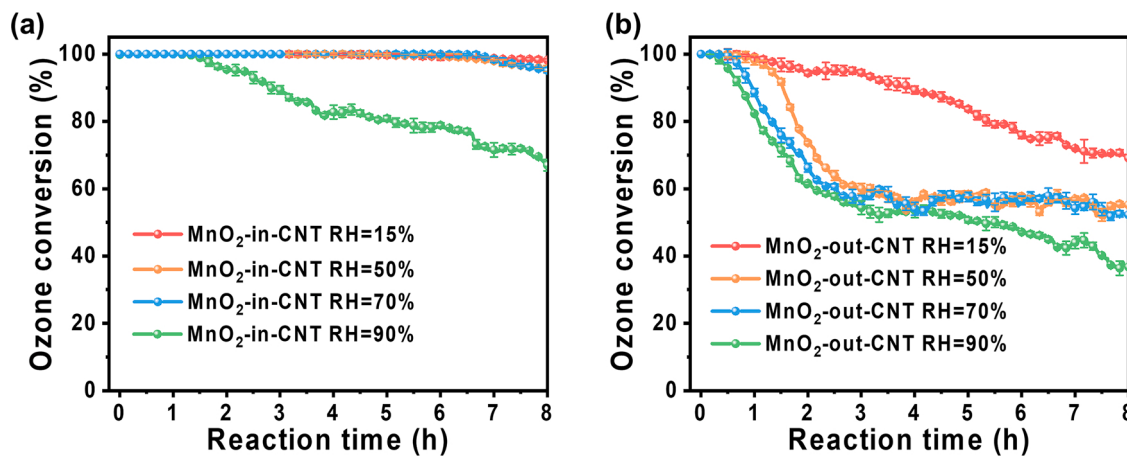


Fig. 3. Ozone conversion on (a) MnO<sub>2</sub>-in-CNT and (b) MnO<sub>2</sub>-out-CNT under different humidity conditions.

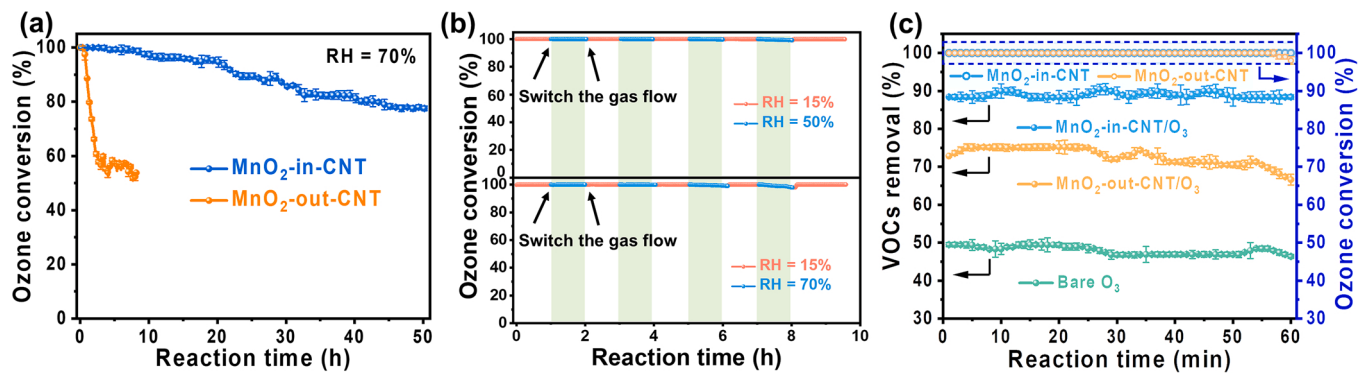


Fig. 4. (a) Ozone conversion performance of MnO<sub>2</sub>-in-CNT and MnO<sub>2</sub>-out-CNT under 70% RH. (b) Ozone conversion performance on MnO<sub>2</sub>-in-CNT at alternate relative humidity (15% RH and 50% RH, 15% RH and 70% RH). (c) Simultaneous removal of VOCs and O<sub>3</sub> in different system.

ambient temperature. We optimized the MnO<sub>2</sub>-in-CNT by adjusting the MnO<sub>2</sub> loading amount from 10 to 30 wt% (Fig. S14). MnO<sub>2</sub>-in-CNT with an optimal MnO<sub>2</sub> loading amount of ca. 20 wt% was used in the following reaction system. As shown in Fig. 2a, the MnO<sub>2</sub>-in-CNT catalyst exhibits 98% persistent ozone conversion efficiency and excellent stability over 100 h under RH of 15%. However, the ozone conversion on MnO<sub>2</sub>-out-CNT catalyst sharply decrease to only 70% after 8 h (Fig. 2b), which could be due to the accumulation of intermediate oxygen species on MnO<sub>2</sub>-out-CNT. The result reveals the remarkable enhanced activity of the MnO<sub>2</sub> particles inside compared with those deposit outside the CNT. The bare MnO<sub>2</sub> sample gives only an ozone conversion below 20% after 8 h. Although the CNT shows good initial catalytic activity (100%), the conversion rate dramatically drops to 17% at 1 h, which might be ascribed to the adsorption saturation of O<sub>3</sub> [34, 35].

Nevertheless, manganese-based catalysts inevitably suffered serious deactivation under humid ozone atmosphere due to the poisoning of water molecules [11, 36, 37]. Therefore, the ozone decomposition performance under high-humidity conditions was explored. As shown in Fig. 3, MnO<sub>2</sub>-in-CNT achieved nearly 100% ozone decomposition efficiency both at 15%, 50%, and 70% RH after 8 h, and the efficiency remained stable even after continuous reaction at 70% RH for 50 h (Fig. 4a), while the ozone conversion on MnO<sub>2</sub>-out-CNT decreased drastically from 70% to 55% and 52% under RH of 15–50%, and 70%. Moreover, the ozone conversion ratio of MnO<sub>2</sub>-in-CNT can be stabilized at 100% under the humidity recycle from 50% to 15% and from 70% to 15%. Even when the humidity decreases from 90% to 15%, the ozone conversion efficiency of MnO<sub>2</sub>-in-CNT can still be quickly recovered to 100% (Fig. 4b and S16), which suggestss the regeneration can easily

occur under alternate humidity conditions reveals the weak adsorption of H<sub>2</sub>O on the MnO<sub>2</sub>-in-CNT. The H<sub>2</sub>O-TPD was further investigated to identify the H<sub>2</sub>O adsorption on the catalyst surface. As shown in Fig. S17, compared with MnO<sub>2</sub>-out-CNT and MnO<sub>2</sub>, the MnO<sub>2</sub>-in-CNT demonstrates the lower adsorption capacity of water, indicating the adsorption of water is hindered on MnO<sub>2</sub>-in-CNT. And the FTIR spectra of samples at dry and humidity were investigated (Fig. S18), the peak of adsorbed water (3464 cm<sup>-1</sup>) on samples were enhanced under moisture, but the weaker changes in the MnO<sub>2</sub>-in-CNT sample was observed, which further indicates that the adsorption of water is hindered on MnO<sub>2</sub>-in-CNT. CNT hosts may act as nanoreactors to decrease the direct contact of interior MnO<sub>2</sub> with water vapor. These results collectively the CNT framework alleviates the effect of water vapour on the ozone conversion on MnO<sub>2</sub>-in-CNT and also makes catalyst regeneration much easier. The ozone decomposition performance in terms of O<sub>3</sub> conversion, GHSV, RH and reaction time in our system was compared to that in other works reported in the literature (Table S1 and S2). Notably, the MnO<sub>2</sub>-in-CNT offers long-term durability and water tolerance that exceed most reported studies.

To further highlight the potential of MnO<sub>2</sub>-in-CNT catalyst for the air purification, we carried out the simultaneous catalytic destruction of VOCs (CH<sub>3</sub>SH) and ozone, which had an original CH<sub>3</sub>SH of 40 ppm and ozone of 50 ppm. As shown in Fig. 4d, the MnO<sub>2</sub>-in-CNT achieved highly stable removal efficiency (90% for 40 ppm of CH<sub>3</sub>SH and 100% for 50 ppm of O<sub>3</sub>) under a GHSV of 120,000 mL h<sup>-1</sup> g<sup>-1</sup>, obviously beyond the MnO<sub>2</sub>-out-CNT catalyst (67% for CH<sub>3</sub>SH and 98% for O<sub>3</sub>) and ozone alone (46% for CH<sub>3</sub>SH), indicating the high activity of MnO<sub>2</sub>-in-CNT to simultaneously eliminate VOCs and ozone under ambient temperature. The above experimental results reveal MnO<sub>2</sub>-in-CNT catalyst possesses

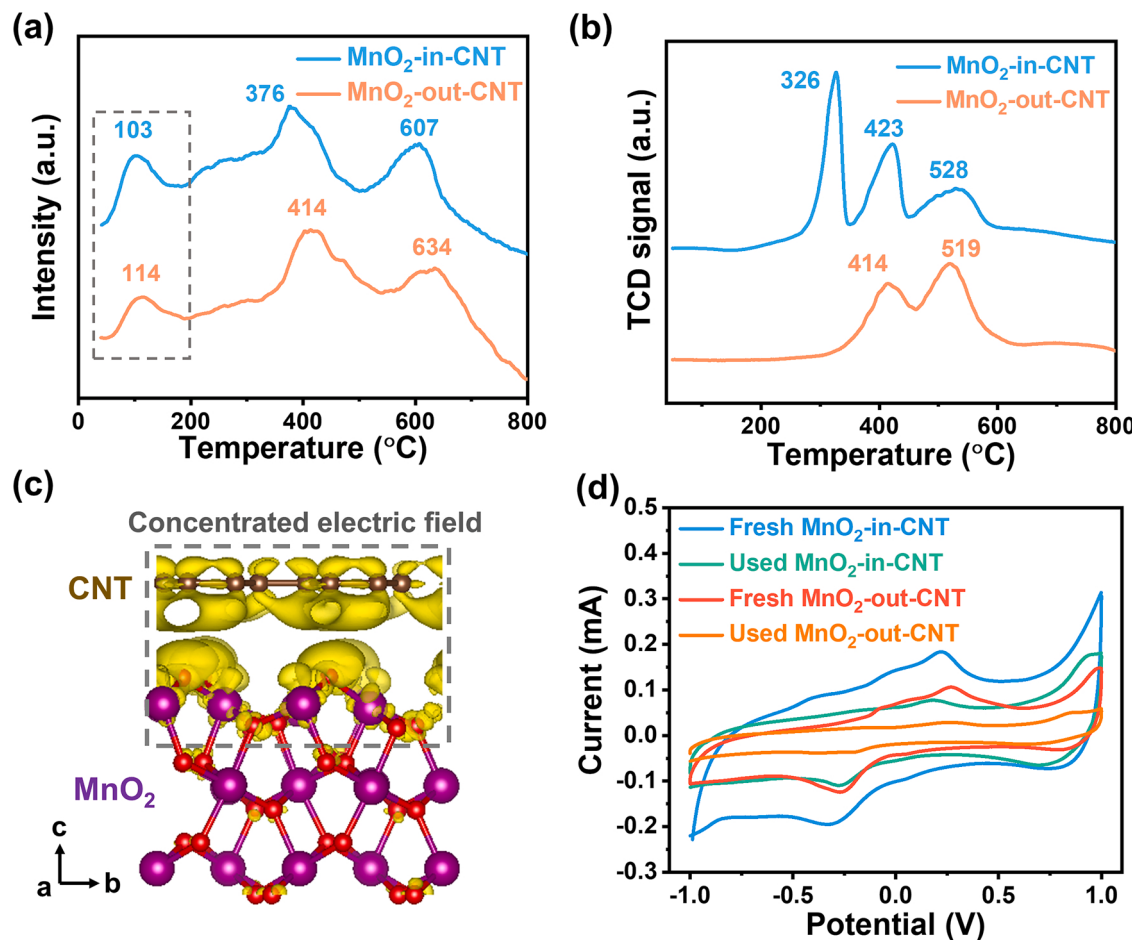


**Fig. 5.** (a) O<sub>2</sub>-TPD profiles and (b) H<sub>2</sub>-TPR profiles of MnO<sub>2</sub>-in-CNT and MnO<sub>2</sub>-out-CNT. (c) Charge density difference diagrams of MnO<sub>2</sub>-in-CNT. (d) CV curves of fresh and used MnO<sub>2</sub>-in-CNT and MnO<sub>2</sub>-out-CNT.

an efficient and robust redox activity, and outstanding water tolerance that shows promising application potential toward ozone elimination, as well as great potential for purification of complex air pollution.

### 3.3. Identification of active sites

Identification of the active sites is essential for understanding the catalytic behavior. Hence, we conducted the O<sub>2</sub> temperature programming desorption (O<sub>2</sub>-TPD), H<sub>2</sub> temperature programmed reduction experiments (H<sub>2</sub>-TPR), DFT calculations, and Cyclic voltammetry (CV) to observe the active sites and redox ability of MnO<sub>2</sub>-in-CNT. The mobility of oxygen species in samples was analyzed by O<sub>2</sub>-TPD. As shown in Fig. 5a, the peaks at 103 °C of MnO<sub>2</sub>-in-CNT can be attributed to the desorption of weak adsorbed oxygens, which can be corresponded to the peroxides desorption from Mn active sites in the step (3) (Eq. 3) [38]. Noteworthy, the MnO<sub>2</sub>-in-CNT demonstrates lower oxygen desorption temperature of the oxygen and larger desorption peak area compared to MnO<sub>2</sub>-out-CNT, revealing the confined structure compromised the energy barriers of oxygen desorption step, which is greatly helpful for accelerating the rate-determining step (peroxide species desorption, Eq. 3) in ozone decomposition. In the medium-temperature (350–600 °C), the MnO<sub>2</sub>-in-CNT sample exhibits lower desorption temperature than MnO<sub>2</sub>-out-CNT indicate the higher activity and mobility of lattice oxygen in MnO<sub>2</sub>-in-CNT, which is beneficial to the redox reactions [9,39,40]. The results of H<sub>2</sub>-TPR are shown in Fig. 5b, three reduction peaks at 326, 423 and 528 °C were observed in MnO<sub>2</sub>-in-CNT, which can be assigned to the reduction of MnO<sub>2</sub> to Mn<sub>2</sub>O<sub>3</sub>, Mn<sub>2</sub>O<sub>3</sub> to Mn<sub>3</sub>O<sub>4</sub> and Mn<sub>3</sub>O<sub>4</sub> to MnO, respectively [41,42]. The reduction peaks of

MnO<sub>2</sub>-out-CNT located at 414 and 519 °C that are higher compared to that of MnO<sub>2</sub>-in-CNT, indicating the MnO<sub>2</sub>-in-CNT owns stronger reducibility and higher mobility of oxygen species than MnO<sub>2</sub>-out-CNT, which is important for the ozonolysis reaction.

The electronic structure within MnO<sub>2</sub>-in-CNT was simulated by the charge density difference calculation (Fig. 5c). Interestingly, the charge-density differences demonstrate that most electrons concentrated in the confined space between the inner MnO<sub>2</sub> and interior wall of CNT, with a fraction of electrons accumulate at the exterior wall of the nearby CNT, revealing the electron-rich sites mainly located at the confined space of MnO<sub>2</sub>-in-CNT due to confinement effect, and the nearby exterior walls of CNT also can be the active sites. It is reported the electrons can be transferred from the Mn exposure site (oxygen vacancy) to the nearby graphene layer and correspondingly an electron-rich site can be formed at the nearby surface of graphene [19]. Given that the similar properties of graphene and CNT, the electrons of Mn atoms in MnO<sub>2</sub>-in-CNT also can be transferred to the nearby exterior walls of CNT. O<sub>3</sub> is an electrophilic molecule, which is readily adsorbed and reacts at sites with high electron density [43]. As shown in the C 1 s spectra of XPS of MnO<sub>2</sub>-in-CNT (Fig. S19), the peak of C=O and C-O slightly increased after being treated with ozone due to a fraction of the carbon surface of CNT shells were oxidized to C=O groups and COOH groups, revealing the ozonation process also appears on the CNT shells of MnO<sub>2</sub>-in-CNT. Furthermore, the electron mobility in the catalysts was evaluated by CV curves. As shown in Fig. 5d, the current of MnO<sub>2</sub>-in-CNT is much higher than that of MnO<sub>2</sub>-out-CNT, proving the stronger electron transfer ability of MnO<sub>2</sub>-in-CNT [44]. It's worth noting that the relatively weaker change in the current intensity of MnO<sub>2</sub>-in-CNT after ozone-catalytic

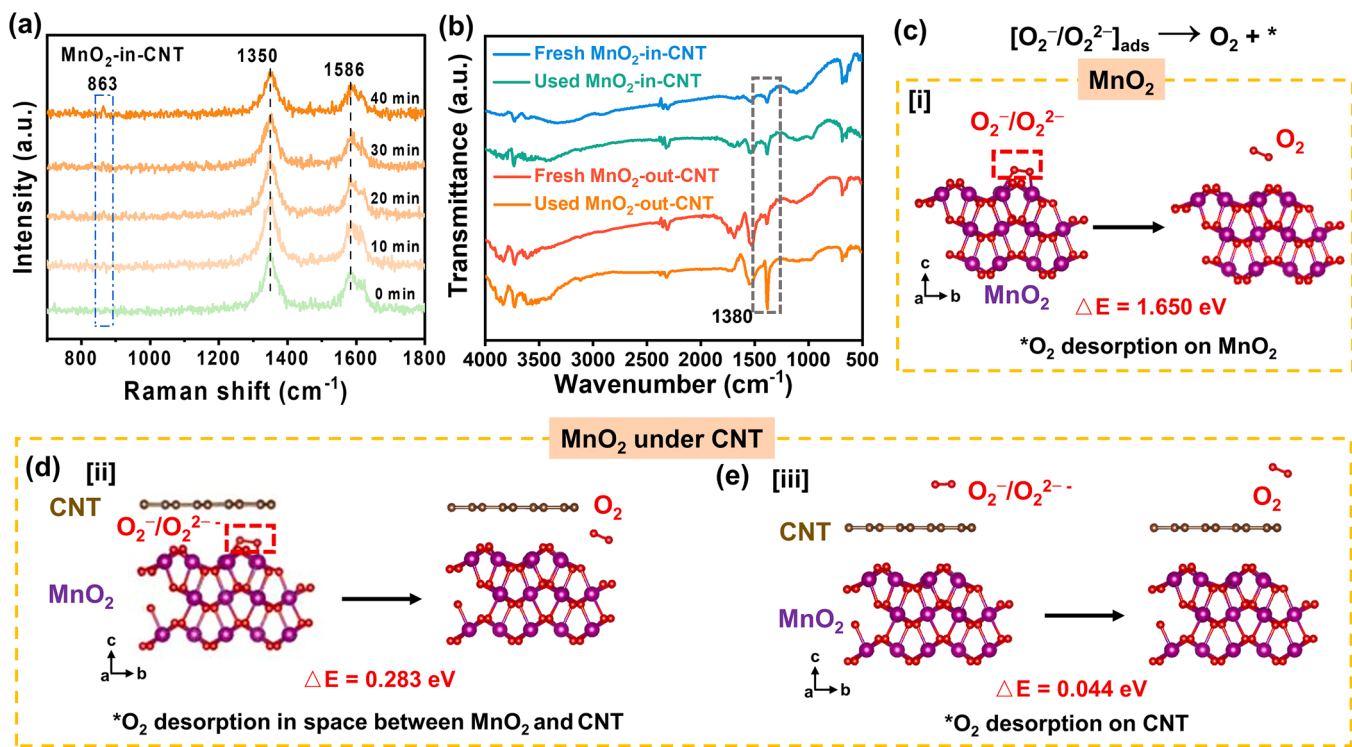


**Fig. 6.** (a) In situ Raman spectra of MnO<sub>2</sub>-in-CNT with 40 min continuous O<sub>3</sub> flow passing at room temperature (25 °C). (b) FTIR spectra of fresh and used MnO<sub>2</sub>-in-CNT and MnO<sub>2</sub>-out-CNT. (c) \*O<sub>2</sub> desorption energy on exposed MnO<sub>2</sub>. (d, e) \*O<sub>2</sub> desorption energy on MnO<sub>2</sub>-in-CNT.

reaction compare with that of MnO<sub>2</sub>-out-CNT was demonstrated, indicating the stronger electron compensation ability in MnO<sub>2</sub>-in-CNT which could enhance the long-term catalytic stability. Moreover, it has been reported that the electrons can transfer from the enclosed catalysts to the carbon shells in the confined-structure catalyst and further penetrate through the interior CNT shell to exterior of CNT based on the results of the C K-edge XANES, STXM, and DFT calculation [45]. Hence, the ozone-catalytic decomposition takes place both inside and outside of CNT in MnO<sub>2</sub>-in-CNT. Considering the reaction on CNT shell also can take place on MnO<sub>2</sub>-out-CNT but the significantly poorer catalytic performance than MnO<sub>2</sub>-in-CNT, it can be deduced the surface of MnO<sub>2</sub> in the confined space should be the main active sites in MnO<sub>2</sub>-in-CNT that enhanced the ozone decomposition. The confined configuration provides MnO<sub>2</sub>-in-CNT with a better redox activity, which is crucial for the ozone-catalytic decomposition.

### 3.4. Ozone conversion mechanism on MnO<sub>2</sub>-in-CNT

Based on the above understanding, reaction intermediates were further analyzed by in situ Raman, FTIR and ESR to explore the ozone reaction mechanism on MnO<sub>2</sub>-in-CNT. As shown in Fig. 6a, with continuous O<sub>3</sub> flow, a new peak was observed at 863 cm<sup>-1</sup>, which was attributed to peroxide (O<sub>2</sub><sup>2-</sup>) [18,38]. It is worth noting that the increase of the peak intensity in MnO<sub>2</sub>-in-CNT is weaker than that in MnO<sub>2</sub>-out-CNT (Fig. S20). This indicates that the accumulation of O<sub>2</sub><sup>2-</sup> is reduced on MnO<sub>2</sub>-in-CNT compared with MnO<sub>2</sub>-out-CNT. In the FTIR spectra (Fig. 6b), the peak at 1380 cm<sup>-1</sup> associated with the free O<sub>2</sub> [46] can be observed in both MnO<sub>2</sub>-in-CNT and MnO<sub>2</sub>-out-CNT, the surface O<sub>2</sub> comes from the O<sub>2</sub> accumulated on surface that derived from the desorbed peroxide species (O<sub>2</sub><sup>\*</sup> → O<sub>2</sub> + \*). Moreover, the peak intensity of surface O<sub>2</sub> in used MnO<sub>2</sub>-in-CNT is much weaker than that of used MnO<sub>2</sub>-out-CNT, which can also indicate that the desorption of O<sub>2</sub><sup>2-</sup> on MnO<sub>2</sub>-in-CNT is easier than that of MnO<sub>2</sub>-out-CNT. As shown in Fig. S21, the signal of O<sub>2</sub><sup>2-</sup> was also detected in the MnO<sub>2</sub>-in-CNT system, where the intensity is higher than that of MnO<sub>2</sub>-out-CNT, relating to \*O<sub>2</sub>

transferring electrons to catalyst to release O<sub>2</sub><sup>2-</sup>. These results confirmed the reduced accumulation of peroxide on MnO<sub>2</sub>-in-CNT compared with unconfined analog.

DFT calculations were used to investigate the energy barrier of rate-determining step (\*O<sub>2</sub> desorption) on the catalyst surface (Fig. 6c-e). Based on the results of active sites identification, we monitored the \*O<sub>2</sub> desorption process (i) on the single MnO<sub>2</sub> (Fig. 6c), (ii) on the surface of MnO<sub>2</sub> in the confined space (Fig. 6d), and (iii) on the exterior wall of carbon shell in the system of MnO<sub>2</sub> under a carbon shell (Fig. 6e). The calculation results reveal the O<sub>3</sub> molecules are prone to attach on MnO<sub>2</sub> rather than on carbon shell. Moreover, the desorption barrier of \*O<sub>2</sub> attached on the exterior wall of a carbon shell (iii) and that in the confined space between MnO<sub>2</sub> and carbon shell (ii) are 0.04 and 0.28 eV, respectively, which is significantly lower than that of \*O<sub>2</sub> on exposed MnO<sub>2</sub> (1.7 eV, (i)), and also lower than the reported ozone decomposition catalyst that has realized accelerated \*O<sub>2</sub> desorption [38]. In the MnO<sub>2</sub>-in-CNT system, the process (ii) could happen on the surface of MnO<sub>2</sub> in the confine space, and process (iii) could happen on the external wall of the CNT, while (ii) should be the main \*O<sub>2</sub> desorption process due to the electronic structure in MnO<sub>2</sub>-in-CNT system. (i) should be the main \*O<sub>2</sub> desorption process in the MnO<sub>2</sub>-out-CNT system with a slight proportion of process (iii) happens on CNT due to the higher affinity of O<sub>3</sub> on MnO<sub>2</sub>. \*O<sub>2</sub> desorption process in the bare MnO<sub>2</sub> is shown as process (i). These results revealed the weakened bonding of \*O<sub>2</sub> in MnO<sub>2</sub>-in-CNT. The stronger electronic interaction between the inner MnO<sub>2</sub> and the interior wall of the CNT modulates its binding energies with \*O<sub>2</sub> [47]. Meanwhile, the significantly compromised reaction barrier on the exterior wall of carbon (0.04 eV) could be attributed to the transfer of interfacial electron from Mn atoms to the nearby carbon shell that effectively modifies the surface electronic properties, which gives the catalyst a moderate local work function to facilitate the desorption of the \*O<sub>2</sub> [19]. The DFT results coincide well with the results observed by O<sub>2</sub>-TPD, ESR and FTIR, confirming the rate-determining step of peroxide species desorption is easier to occur on MnO<sub>2</sub>-in-CNT, thereafter releasing more available active sites for

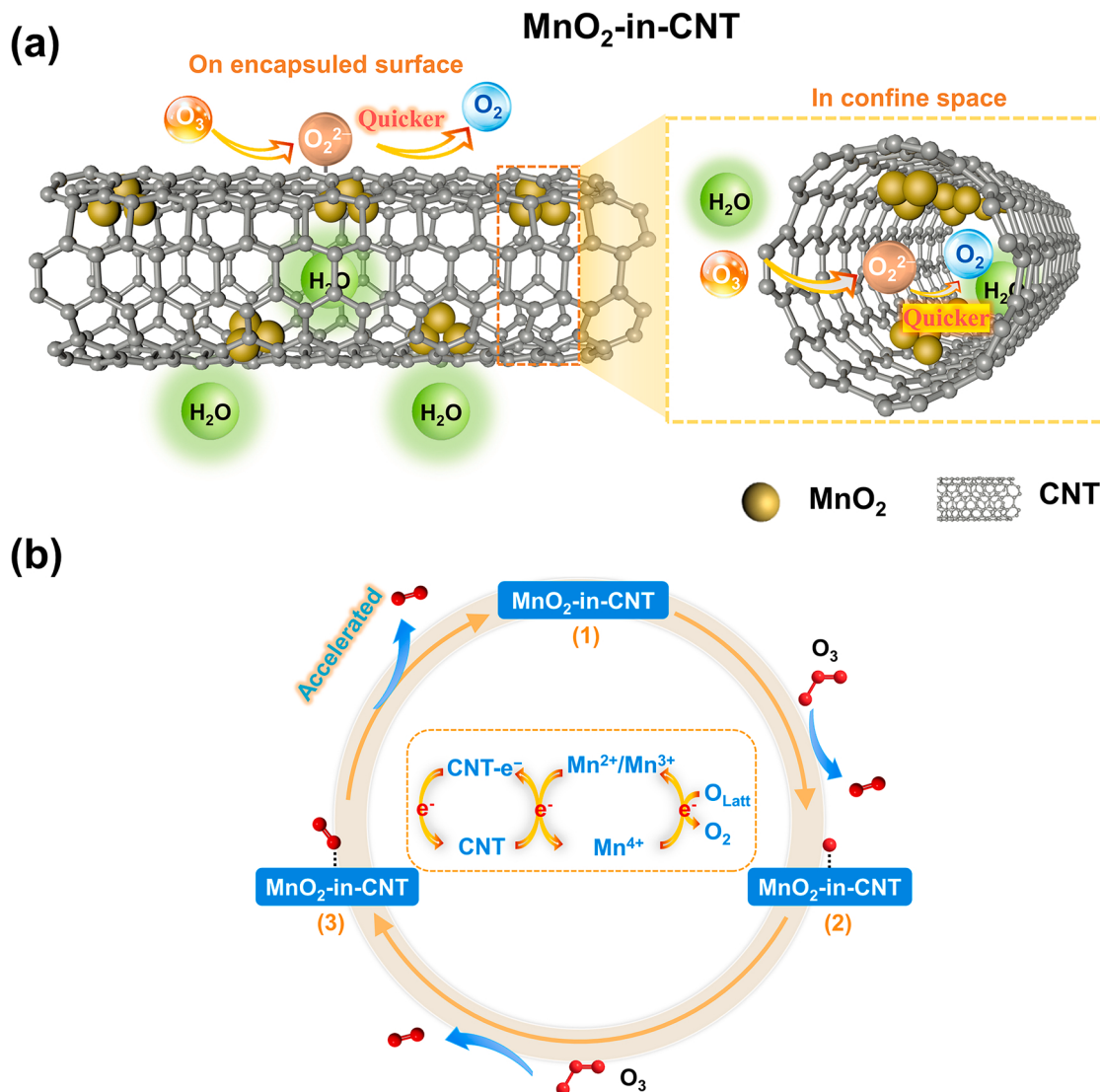


**Fig. 7.** (a) The schematic diagram of ozone decomposition on  $MnO_2$ -in-CNT. (b) The reaction mechanism of ozone decomposition on  $MnO_2$ -in-CNT.

accelerating the ozone decomposition and realizing impressive stability in long-term.

According to the above performances and calculations, the ozone decomposition mechanism over the  $MnO_2$ -in-CNT system is proposed. As shown in Fig. 7a and Fig. S22, ozone molecules diffuse into the carbon nanotubes of  $MnO_2$ -in-CNT and the ozone decomposition over  $MnO_2$ -in-CNT on the surface of the  $MnO_2$  in the confined space are the main reactive sites, where the oxygen vacancies in  $MnO_2$  should play the main role [16]. Meanwhile, CNT can be activated by the electron transferred from the nearby Mn atoms, thereby partial ozone molecules attach on the exterior wall of CNT and are catalyzed. As shown in Fig. 7b, ozone molecules are dissociative adsorbed on those active sites and are catalyzed to form oxygen molecules and oxygen species ( $^*O$ ). The  $^*O$  will continue to react with another ozone molecule to form peroxide species ( $^*O_2$ ). Eventually, the  $^*O_2$  desorbed from catalyst to release  $O_2$  and  $O_2^{2-}$  after transferring electron back to catalyst (Fig. S23 and Table S3), which is the rate-determining step of ozonolysis. This rate-determining step occurs more easily on  $MnO_2$ -in-CNT compared to  $MnO_2$  attributing to the confined-structure merits. Meanwhile, confinement of  $MnO_2$  within CNTs greatly decreased the direct contact of interior  $MnO_2$  with water vapor, enabling the  $MnO_2$ -in-CNT catalyst to maintain an efficient and robust ozone decomposition performance under high humidity.

#### 4. Conclusion

Our work has presented a space-confined catalyst using interface electronic modulation ( $MnO_2$ -in-CNT) to achieve exceptional ozone decomposition activity, impressive stability in long-term and moisture suitability, and provided a mechanistic understanding of the confined-structure merits on ozone decomposition. Moreover, this confinement system can also simultaneously decompose  $O_3$  and VOCs to achieve air purification. Combining experimental characterizations and DFT calculations, it is observed that the ozone decomposition on  $MnO_2$ -in-CNT exhibited undermined barriers of rate-determining step of ozone decomposition. Meanwhile, the confined structure alleviated the effect of water vapor on ozone conversion. This cost-effective system with high activity, impressive stability and humidity tolerance is expected can be applied to reduce ground-level ozone. We hope our work could stimulate the researchers to develop efficient dimensionally confined catalysts for various air pollution applications to improve the atmospheric environment.

#### CRediT authorship contribution statement

**Bin Liu:** Data curation, Formal analysis, Methodology, Writing – original draft. **Ziran Yi:** Investigation, Data curation. **Yunjun Yang:**

**Investigation, Data curation. Yatai Li:** Investigation, Data curation. **Jingling Yang:** Conceptualization, Data curation, Methodology, Funding acquisition, Supervision, Writing – review & editing. **Mingshan Zhu:** Conceptualization, Funding acquisition, Supervision, Writing – review & editing.

## Data Availability

Data will be made available on request.

## Acknowledgments

The study was financially supported by the National Natural Science Foundation of China (No. 22006051), the Guangdong Basic Applied Basic Research Foundation (No. 2022A1515010655), Pearl River Talent Recruitment Program of Guangdong Province (No. 2021QN020272), and the Science and Technology Program of Guangzhou (No. 202102020325).

## Conflicts of interest

There are no conflicts of interest to declare.

## Appendix A. Supporting information

Supplementary data associated with this article can be found in the online version at [doi:10.1016/j.apcatb.2023.122788](https://doi.org/10.1016/j.apcatb.2023.122788).

## References

- [1] N. Unger, Y. Zheng, X. Yue, K.L. Harper, Mitigation of ozone damage to the world's land ecosystems by source sector, *Nat. Clim. Change* 10 (2020) 134–137.
- [2] X. Lu, J. Hong, L. Zhang, O.R. Cooper, M.G. Schultz, X. Xu, T. Wang, M. Gao, Y. Zhao, Y. Zhang, Severe surface ozone pollution in china: Aa global perspective, *Environ. Sci. Technol. Lett.* 5 (2018) 487–494.
- [3] O.R. Cooper, D.D. Parrish, A. Stohl, M. Trainer, P. Nédélec, V. Thouret, J. P. Cammas, S.J. Oltmans, B.J. Johnson, D. Tarasick, T. Leblanc, I.S. McDermid, D. Jaffe, R. Gao, J. Stith, T. Ryerson, K. Aikin, T. Campos, A. Weinheimer, M. A. Avery, Increasing springtime ozone mixing ratios in the free troposphere over western North America, *Nature* 463 (2010) 344–348.
- [4] R.R. Dickerson, S. Kondragunta, G. Stenchikov, K.L. Civerolo, B.G. Doddridge, B. N. Holben, The impact of aerosols on solar ultraviolet radiation and photochemical smog, *Science* 278 (1997) 827–830.
- [5] H. Li, S. Wu, L. Pan, J. Xu, J. Shan, X. Yang, W. Dong, F. Deng, Y. Chen, M. Shima, X. Guo, Short-term effects of various ozone metrics on cardiopulmonary function in chronic obstructive pulmonary disease patients: results from a panel study in Beijing, China, *Environ. Pollut.* 232 (2018) 358–366.
- [6] D. Berman Jesse, N. Fann, W. Hollingsworth John, E. Pinkerton Kent, N. Rom William, M. Szema Anthony, N. Breyses Patrick, H. White Ronald, C. Curriero Frank, Health benefits from large-scale ozone reduction in the united states, *Environ. Health Perspect.* 120 (2012) 1404–1410.
- [7] B. Hoffmann, H. Luttmann-Gibson, A. Cohen, A. Zanobetti, C. de Souza, C. Foley, H. Suh Helen, A. Coull Brent, J. Schwartz, M. Mittleman, P. Stone, E. Horton, R. Gold Diane, Opposing effects of particle pollution, ozone, and ambient temperature on arterial blood pressure, *Environ. Health Perspect.* 120 (2012) 241–246.
- [8] X. Li, J. Ma, H. He, Recent advances in catalytic decomposition of ozone, *J. Environ. Sci.* 94 (2020) 14–31.
- [9] J. Jia, P. Zhang, L. Chen, Catalytic decomposition of gaseous ozone over manganese dioxides with different crystal structures, *Appl. Catal. B: Environ.* 189 (2016) 210–218.
- [10] J. Ma, C. Wang, H. He, Transition metal doped cryptomelane-type manganese oxide catalysts for ozone decomposition, *Appl. Catal. B: Environ.* 201 (2017) 503–510.
- [11] C. Wang, J. Ma, F. Liu, H. He, R. Zhang, The effects of Mn<sup>2+</sup> precursors on the structure and ozone decomposition activity of cryptomelane-type manganese oxide (OMS-2, ) *Catal., J. Phys. Chem. C.* 119 (2015) 23119–23126.
- [12] Y. Yu, S. Liu, J. Ji, H. Huang, Amorphous MnO<sub>2</sub> surviving calcination: an efficient catalyst for ozone decomposition, *Catal. Sci. Technol.* 9 (2019) 5090–5099.
- [13] J.-M. Tatibouët, S. Valange, H. Touati, Near-ambient temperature ozone decomposition kinetics on manganese oxide-based catalysts, *Appl. Catal. A: Gen.* 569 (2019) 126–133.
- [14] L. Zhang, J. Yang, A. Wang, S. Chai, J. Guan, L. Nie, G. Fan, N. Han, Y. Chen, High performance ozone decomposition spinel (Mn,Co)<sub>3</sub>O<sub>4</sub> catalyst accelerating the rate-determining step, *Appl. Catal. B: Environ.* 303 (2022), 120927.
- [15] W. Li, G.V. Gibbs, S.T. Oyama, Mechanism of ozone decomposition on a manganese oxide catalyst. I. In situ raman spectroscopy and ab initio molecular orbital calculations, *J. Am. Chem. Soc.* 120 (1998) 9041–9046.
- [16] G. Zhu, J. Zhu, W. Li, W. Yao, R. Zong, Y. Zhu, Q. Zhang, Tuning the K<sup>+</sup> concentration in the tunnels of α-MnO<sub>2</sub> to increase the content of oxygen vacancy for ozone elimination, *Environ. Sci. Technol.* 52 (2018) 8684–8692.
- [17] S. Liu, J. Ji, Y. Yu, H. Huang, Facile synthesis of amorphous mesoporous manganese oxides for efficient catalytic decomposition of ozone, *Catal. Sci. Technol.* 8 (2018) 4264–4273.
- [18] Z.-B. Sun, Y.-N. Si, S.-N. Zhao, Q.-Y. Wang, S.-Q. Zang, Ozone decomposition by a manganese-organic framework over the entire humidity range, *J. Am. Chem. Soc.* 143 (2021) 5150–5157.
- [19] G. Zhu, W. Zhu, Y. Lou, J. Ma, W. Yao, R. Zong, Y. Zhu, Encapsulate α-MnO<sub>2</sub> nanofiber within graphene layer to tune surface electronic structure for efficient ozone decomposition, *Nat. Commun.* 12 (2021) 4152.
- [20] E. Castillejos, P.-J. Debouttière, L. Roiban, A. Solhy, V. Martinez, Y. Kihn, O. Ersen, K. Philippot, B. Chaudret, P. Serp, An efficient strategy to drive nanoparticles into carbon nanotubes and the remarkable effect of confinement on their catalytic performance, *Angew. Chem. Int. Ed.* 48 (2009) 2529–2533.
- [21] X. Yang, J.-K. Sun, M. Kitta, H. Pang, Q. Xu, Encapsulating highly catalytically active metal nanoclusters inside porous organic cages, *Nat. Catal.* 1 (2018) 214–220.
- [22] J. Xiao, X. Pan, S. Guo, P. Ren, X. Bao, Toward fundamentals of confined catalysis in carbon nanotubes, *J. Am. Chem. Soc.* 137 (2015) 477–482.
- [23] N. Wang, Q. Sun, J. Yu, Ultrasmall metal nanoparticles confined within crystalline nanoporous materials: a fascinating class of nanocatalysts, *Adv. Mater.* 31 (2019), 1803966.
- [24] W. Chen, Z. Fan, X. Pan, X. Bao, Effect of confinement in carbon nanotubes on the activity of fischer–tropsch iron catalyst, *J. Am. Chem. Soc.* 130 (2008) 9414–9419.
- [25] X. Zheng, J. Xu, K. Yan, H. Wang, Z. Wang, S. Yang, Space-confined growth of MoS<sub>2</sub> nanosheets within graphite: the layered hybrid of MoS<sub>2</sub> and graphene as an active catalyst for hydrogen evolution reaction, *Chem. Mater.* 26 (2014) 2344–2353.
- [26] F.L. De Volder Michael, H. Tawfick Sameh, H. Baughman Ray, A.J. Hart, Carbon nanotubes: present and future commercial applications, *Science* 339 (2013) 535–539.
- [27] X. Pan, Z. Fan, W. Chen, Y. Ding, H. Luo, X. Bao, Enhanced ethanol production inside carbon-nanotube reactors containing catalytic particles, *Nat. Mater.* 6 (2007) 507–511.
- [28] Z. Yang, J. Qian, A. Yu, B. Pan, Singlet oxygen mediated iron-based Fenton-like catalysis under nanoconfinement, *Proc. Natl. Acad. Sci.* 116 (2019) 6659–6664.
- [29] S. Chen, G. Wu, M. Sha, S. Huang, Transition of ionic liquid [bmim][PF6] from liquid to high-melting-point crystal when confined in multiwalled carbon nanotubes, *J. Am. Chem. Soc.* 129 (2007) 2416–2417.
- [30] W. Chen, Z. Fan, L. Gu, X. Bao, C. Wang, Enhanced capacitance of manganese oxide via confinement inside carbon nanotubes, *Chem. Commun.* 46 (2010) 3905–3907.
- [31] W. Chen, X. Pan, X. Bao, Tuning of redox properties of iron and iron oxides via encapsulation within carbon nanotubes, *J. Am. Chem. Soc.* 129 (2007) 7421–7426.
- [32] P.C. Eklund, J.M. Holden, R.A. Jishi, Vibrational modes of carbon nanotubes; spectroscopy and theory, *Carbon* 33 (1995) 959–972.
- [33] C. Xu, S. Shi, Y. Sun, Y. Chen, F. Kang, Ultrathin amorphous manganese dioxide nanosheets synthesized with controllable width, *Chem. Commun.* 49 (2013) 7331–7333.
- [34] H. Wang, P. Rassu, X. Wang, H. Li, X. Wang, X. Feng, A. Yin, P. Li, X. Jin, S.-L. Chen, X. Ma, B. Wang, An iron-containing metal-organic framework as a highly efficient catalyst for ozone decomposition, *Angew. Chem. Int. Ed.* 57 (2018) 16416–16420.
- [35] S. Yang, J. Nie, F. Wei, X. Yang, Removal of ozone by carbon nanotubes/quartz fiber film, *Environ. Sci. Technol.* 50 (2016) 9592–9598.
- [36] A. Naydenov, P. Konova, P. Nikolov, F. Klingstedt, N. Kumar, D. Kovacheva, P. Stefanov, R. Stoyanova, D. Mehandjiev, Decomposition of ozone on Ag/SiO<sub>2</sub> catalyst for abatement of waste gases emissions, *Catal. Today* 137 (2008) 471–474.
- [37] B. Liu, M. Zhang, J. Yang, M. Zhu, Efficient ozone decomposition over bifunctional Co<sub>3</sub>Mn-layered double hydroxide with strong electronic interaction, *Chin. Chem. Lett.* 33 (2022) 4679–4682.
- [38] X. Wan, L. Wang, S. Zhang, H. Shi, J. Niu, G. Wang, W. Li, D. Chen, H. Zhang, X. Zhou, W. Wang, Ozone decomposition below room temperature using Mn-based mullite YMn<sub>2</sub>O<sub>5</sub>, *Environ. Sci. Technol.* 56 (2022) 8746–8755.
- [39] N. Dong, Q. Ye, Y. Xiao, D. Zhang, H. Dai, Enhancement in catalytic performance of birnessite-type MnO<sub>2</sub>-supported Pd nanoparticles by the promotional role of reduced graphene oxide for toluene oxidation, *Catal. Sci. Technol.* 12 (2022) 2197–2209.
- [40] J. Ye, M. Zhou, Y. Le, B. Cheng, J. Yu, Three-dimensional carbon foam supported MnO<sub>2</sub>/Pt for rapid capture and catalytic oxidation of formaldehyde at room temperature, *Appl. Catal. B: Environ.* 267 (2020), 118689.
- [41] X. Li, J. Ma, H. He, Tuning the chemical state of silver on Ag–Mn catalysts to enhance the ozone decomposition performance, *Environ. Sci. Technol.* 54 (2020) 11566–11575.
- [42] L. Zhang, J. Yang, A. Wang, S. Chai, J. Guan, L. Nie, G. Fan, N. Han, Y. Chen, High performance ozone decomposition spinel (Mn,Co)<sub>3</sub>O<sub>4</sub> catalyst accelerating the rate-determining step, *Appl. Catal. B: Environ.* 303 (2022), 120927.
- [43] D. Xia, W. Xu, Y. Wang, J. Yang, Y. Huang, L. Hu, C. He, D. Shu, D.Y.C. Leung, Z. Pang, Enhanced performance and conversion pathway for catalytic ozonation of methyl mercaptan on single-atom Ag deposited three-dimensional ordered mesoporous MnO<sub>2</sub>, *Environ. Sci. Technol.* 52 (2018) 13399–13409.

- [44] D. Ma, W. Liu, Y. Huang, D. Xia, Q. Lian, C. He, Enhanced catalytic ozonation for eliminating CH<sub>3</sub>SH via stable and circular electronic metal–support interactions of Si–O–Mn bonds with low Mn loading, Environ. Sci. Technol. 56 (2022) 3678–3688.
- [45] X. Chen, J. Xiao, J. Wang, D. Deng, Y. Hu, J. Zhou, L. Yu, T. Heine, X. Pan, X. Bao, Visualizing electronic interactions between iron and carbon by X-ray chemical imaging and spectroscopy, Chem. Sci. 6 (2015) 3262–3267.
- [46] K. Kunimatsu, T. Yoda, D.A. Tryk, H. Uchida, M. Watanabe, In situ ATR-FTIR study of oxygen reduction at the Pt/Nafion interface, Phys. Chem. Chem. Phys. 12 (2010) 621–629.
- [47] J. Xiao, X. Pan, F. Zhang, H. Li, X. Bao, Size-dependence of carbon nanotube confinement in catalysis, Chem. Sci. 8 (2017) 278–283.